

On the Influence of Buoyancy Fluxes on Wind Drift Currents

SIGNILD NERHEIM AND ANDERS STIGEBRANDT

Department of Earth Sciences–Oceanography, Göteborg University, Gothenburg, Sweden

(Manuscript received 10 December 2004, in final form 9 December 2005)

ABSTRACT

Data from a moored buoy in the Baltic proper have been analyzed to study the ageostrophic wind-driven (Ekman) transport accounting for buoyancy fluxes in a stratified ocean. A model considering different dynamical regimes governed by wind stress τ , buoyancy fluxes, stratification, and rotation is used to determine the thickness of the mixed layer. For shallow layers in the regime of positive buoyancy fluxes (35% of the time) a transport of about $0.77\tau/\rho f$ directed about 30° to the right of the wind is observed. This is far from $1.0\tau/\rho f$ and 90° , given by the classical Ekman solution for homogeneous water. The result can be understood qualitatively as caused by drag between the well-mixed surface layer and the underlying layer if the time scale of decay is about 2 h^{-1} . For negative buoyancy fluxes through the sea surface (53% of the time) the mean observed transport was $1.69\tau/\rho f$ directed about 60° to the right of the wind. Finite-depth equations for homogeneous water cannot explain this result. No simple explanation of this observational result is offered, but it should be connected to the simultaneously occurring thermohaline convection, which efficiently transmits momentum vertically to the whole mixed layer. The computed mean energy transfer to the wind current is about 12 mW m^{-2} .

1. Introduction

Ekman's classical theory for wind-driven currents is a fundamental part of the theory of ocean circulation. The wind drift in deep homogeneous waters, a vertically integrated volume transport of $\tau/\rho f$ perpendicular to the sea surface wind stress τ (Ekman 1905), is considered robust because of its independence of the vertical distribution of diffusivity. However, more often than not, crucial assumptions of Ekman's theory, such as a nonstratified ocean, are not fulfilled.

Studies of the wind-driven surface transport show an observed transport that at least on average is relatively close to the theoretical Ekman transport, and where the direction of the transport deviates from the wind though not exactly perpendicular (e.g., Davis et al. 1981; Price et al. 1987; Niiler and Paduan 1995; Chereskin 1995). However, the choice of an Ekman layer depth is often ambiguous, or found indirectly from comparison between the theoretical and estimated transport. From autumn and winter measurements near

station P in the Pacific Ocean, where the mixed layer was 60 m thick, Niiler and Paduan (1995) used regression analysis and found an apparent mixing depth of 34–37 m based on comparisons with the theoretical Ekman transport. In the Long-Term Upper-Ocean Study (LOTUS) conducted in the western Sargasso Sea, Price et al. (1987) found that the observed transport was consistent with the theoretical Ekman transport to within 10% and that 95% of the wind-driven transport occurred in the upper 25 m, in fair summer weather. From direct measurements of wind and near-surface currents along a section at 11°N , Chereskin and Roemmich (1991) removed the geostrophic flow and considered the ageostrophic, surface-trapped transport in the upper 100 m. The measured total transport was a factor 1.36 (± 0.25) larger than the transport estimated from shipboard wind (i.e., $\tau/\rho f$). The measurements were taken in late winter under heavier winds than in previous experiments (e.g., Davis et al. 1981; Price et al. 1987), and the penetration depth to which the Ekman balance was found was below the mixed layer depth. During a 6-month (summer) period of moderate, southerly winds Chereskin (1995) found an Ekman balance in the California Current nearly equal to the theoretical result, for both direction and magnitude. Price and Sundermeyer (1999) reviewed questions concerning the im-

Corresponding author address: Signild Nerheim, Department of Earth Sciences–Oceanography, Göteborg University, Box 460, 405 30 Göteborg, Sweden.
E-mail: sine@oce.gu.se

portance of the time-dependent variations in stratification and found a qualitatively realistic Ekman layer structure by incorporating a diurnal cycle in a time-dependent diffusion model. Here, the daily change in mixed layer depth was studied but not the difference in buoyancy forcing.

There is a certain arbitrariness regarding the choice of the wind-current depth in the cited experimental studies. Since the wind power primarily is supplied to the well-mixed surface layer, the wind drift should be confined to this layer. Is the real depth of the wind drift given by the classical Ekman theory? The answer to this question is generally negative because buoyancy fluxes through the sea surface introduce buoyancy effects and stratification. The easiest way to establish the thickness of the well-mixed surface layer is through studies of the thermal and haline response of the mixed layer to the fluxes of heat and freshwater through the sea surface. Obviously, a seasonal pycnocline model cannot satisfactorily compute the evolution of the thermal and haline properties of the surface layer unless the thickness of the well-mixed surface layer is correctly computed.

In the present paper the pycnocline model presented in Stigebrandt (1985) was used to determine the proper layer depth and subsequently analyze current measurements obtained in the open Baltic proper with respect to the wind-driven transport. This model of the depth of the well-mixed surface layer accounts for rotation, sea surface buoyancy fluxes, and stratification. Distinguishing between the depth of the uppermost pycnocline, and for positive buoyancy fluxes through the sea surface, the Ekman depth and the Monin–Obukhov depth, the model successfully computed the depth of the seasonal thermocline and the main halocline of the Baltic by consistently using the shallowest of these depths as the depth of the well-mixed surface layer. During periods of positive buoyancy flux, the smallest of the Monin–Obukhov depth, the Ekman depth, and the depth of the uppermost pycnocline, respectively, is chosen. For negative buoyancy fluxes, the mixed layer depth should be the wind-current depth, as buoyancy-driven convection will distribute momentum from the wind over the whole water column down to the pycnocline. The analysis below thus distinguishes between three dynamical regimes during positive buoyancy flux and one regime for negative buoyancy flux.

Three months of data from a mooring in the north-western Baltic proper are analyzed to establish the dynamics behind the observed current. Hydrography, wind forcing, buoyancy fluxes, and current measurements are used in this study. Looking at the ageostrophic, wind-driven component and using the model of Stigebrandt (1985) the dynamics described by the

buoy data are explored and compared with classical Ekman theory. Section 2 gives a presentation of the data and methods used. In section 3, hydrography, wind, and buoyancy forcing are shown, and in section 4 the current data are presented. In section 5, the wind drift under different dynamical regimes is presented and compared with the theoretical Ekman transport. Section 6 explores possible mechanisms behind the observed transport, followed by concluding remarks in section 7.

2. Data and methods

The dataset is from a buoy deployed in the north-western Baltic proper by the Swedish Institute of Meteorology and Hydrology (SMHI). The buoy position is 58°55'N, 19°09'E (Fig. 1). The distance to the shore exceeds the internal Rossby radius (≈ 10 km) by a factor of 3.

The data have been through a quality control at SMHI. At 2- and 4-m depth, the current was measured by acoustic current meters from Falmouth Scientific, Inc. (ACM-CBA-S). From 12 m down to 90 m, an ADCP (Nortek DP, 500 kHz) mounted on the bottom concrete fundament measured the current speed. The vertical resolution is 4 m between 12 and 48 m, and 10 m between 50 and 90 m.

The recorded currents are a mixture of components of various frequencies and wavenumbers. We want to remove all components that are not part of the primary, local quasi-steady wind drift. High-frequency current components, mainly inertial oscillations, were removed by filtering the current with a Butterworth low-pass filter with cutoff frequency 24 h. The directly wind-forced local component was found by removal of the velocity at a reference depth, in accordance with previous works (e.g., Chereskin and Roemmich 1991; Schudlich and Price 1998). Liljebladh and Stigebrandt (1996) used hydrographic data to remove the calculated baroclinic velocity and found the barotropic reference velocity as the residual at an interior depth. The present dataset does not allow an estimate of the baroclinic velocity, but the general hydrographic conditions in the area were checked using data from the Baltic Environmental Database (BED). The assumption that the removal of the reference velocity is sufficient to isolate the wind-driven part of the current is explained in section 4, together with a discussion of topographic effects.

The buoy records temperature and salinity with conductivity–temperature (CT) sensors from Sea-Bird Electronics at the same depths at which the current is monitored. The salinity data from 2- and 4-m depth were discarded the second half of the period because of instrument failure. However, this is not a problem because temperature profiles indicated that the upper

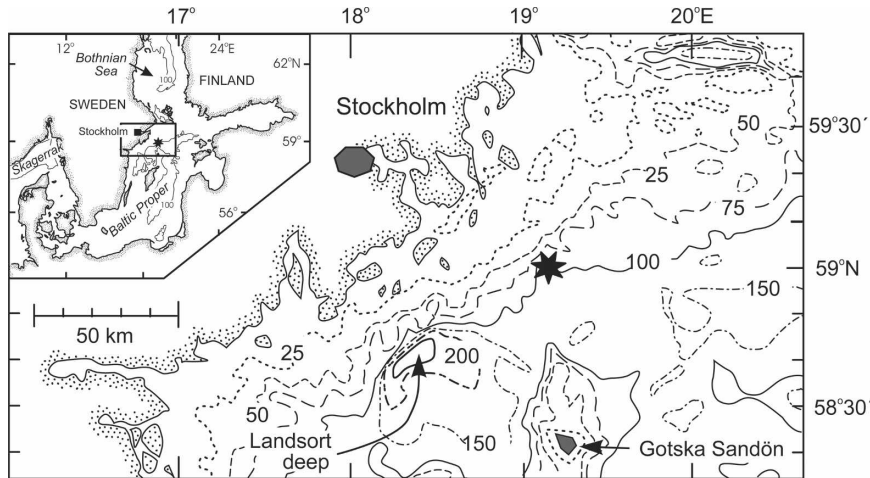


FIG. 1. The Baltic proper with the SMHI mooring (star). The buoy is more than 300 km from the coast, and the water depth is 95 m. The bottom contours are parallel to the coast.

layer was well mixed down to 30–50 m in this period. Wind speed and direction, air temperature and pressure, and wave direction and height were also measured. The air temperature and the wind speed and direction were measured 3.6 m above the sea surface. The wind was filtered with the same low-pass filter as the current for consistency.

The rationale behind the choice of length scales is as follows: The Ekman depth, $h_e = \kappa u_* / f$, is set by the friction velocity u_* , the Coriolis parameter f , and an empirical constant κ . This is the “classical” depth of the wind-driven boundary layer, applicable when buoyancy and stratification effects vanish. For positive buoyancy flux B through the surface, the Monin–Obukhov depth, $h_{mo} = 2m_0 u_*^3 / B$, where m_0 is an empirical constant and B is the buoyancy flux, is the depth to which the wind is able to mix down the added buoyancy and momentum. Stigebrandt (1985) estimated $\kappa = 0.20$ and $m_0 = 0.6$ from the seasonal evolution of temperature and salinity in the Baltic Sea.

To compute the Ekman depth in homogeneous water $h_e = \kappa u_* / f$, and the Monin–Obukhov depth h_{mo} , the friction velocity in the mixed layer, $u_* = \sqrt{\tau / \rho}$, must be known. The wind stress τ was calculated from

$$\tau = C_d \rho_a W^2, \tag{1}$$

where W is the wind speed at a reference height and ρ_a the density of air. The drag coefficient C_d , derived from boundary layer meteorology, is calculated as follows:

$$C_d = \frac{k^2}{[\ln(z_r / z_0) - \Phi_m]^2} \tag{2}$$

where $k = 0.4$ is the von Kármán constant, z_r is the reference height, z_0 is the roughness length for momen-

tum, and Φ_m is the nondimensional gradient of momentum (Arya 1988); Φ_m is a function of the atmospheric stability, expressed as a bulk Richardson number dependent on the air and sea surface temperatures, and the roughness lengths for momentum and heat. The stability-dependent coefficients from Launiainen (1995) and the density ρ_a of dry air were used in the present calculations.

The parameterization of the wind stress introduces a possible bias primarily affecting the amplitude of the transport. For simplicity, wind stress estimates are often based on empirical drag coefficients that depend on wind speed only. The coefficients are most often valid for a neutral atmosphere, and Large and Pond (1981) report a 20% uncertainty in the wind stress estimate from these formulas. A drag coefficient based on boundary layer meteorology incorporates more of the air–sea boundary layer physics and needs only the air and sea surface temperatures as additional parameters. Boundary layer meteorology parameterization [Eq. (2)] improved the model results in the Program for Boundary Layers in the Environment (PROBE) model for the Baltic Sea (A. Omstedt 2005, personal communication). Carlsson (1998) modeled the mean sea level in the Baltic Sea and found that the model was improved by increasing the drag coefficient during winter, when the atmosphere was assumed to be more unstable. To increase the accuracy of the model, Carlsson (1998) suggested that a stability-dependent drag coefficient be used, one that also takes the sea ice condition into account. During the measurements used in the present paper, the air column was stable only for a short period in late June.

To investigate the importance of Monin–Obukhov

dynamics during the observational period one needs to know B , which depends on the fluxes of heat q_{in} and freshwater F_{in} through the sea surface. The buoyancy flux B is given by

$$B = g \frac{\alpha}{\rho c_p} q_{in} + g\beta F_{in} S, \quad (3)$$

with g being the gravitational constant; α and β the thermal expansion and salinity contraction coefficients of seawater, respectively; S the surface salinity; ρ the density of the mixed layer; and c_p the specific heat of water; q_{in} and F_{in} were calculated from the observed changes of the heat and freshwater contents of the mixed layer, including entrainment of waters from below. During periods of pycnocline erosion, q_{in} was found from

$$\begin{aligned} q_{in}\Delta t + \rho c_p \Delta H T_o &= \Delta Q = Q(t + \Delta t) - Q(t) \\ &= \rho c_p [H(t) + \Delta H] T(t + \Delta t) \\ &\quad - \rho c_p H(t) T(t), \end{aligned} \quad (4)$$

where H and ΔH are the mixed layer thickness and the change in mixed layer depth during one time step, respectively; $T(t)$ is the temperature at time t ; T_o is the temperature of entrained waters; $Q(t)$ is the heat content at time t , which gives

$$\begin{aligned} q_{in} &= \frac{\rho c_p}{\Delta t} \{ H [T(t + \Delta t) - T(t)] \\ &\quad + \Delta H [T(t + \Delta t) - T_o] \}; \quad \Delta H \geq 0. \end{aligned} \quad (5)$$

For pycnocline retreat, the heat flux was found from

$$\begin{aligned} q_{in}\Delta t &= \Delta Q \\ &= \rho c_p \left\{ \frac{H(t + \Delta t) + H(t)}{2} [T(t + \Delta t) - T(t)] \right\}, \end{aligned} \quad (6)$$

giving

$$q_{in} \frac{\rho c_p}{\Delta t} \frac{H(t + \Delta t) + H(t)}{2} [T(t + \Delta t) - T(t)]; \quad \Delta H \leq 0. \quad (7)$$

The freshwater flux through the sea surface was determined accordingly, with the freshwater height F calculated from

$$F = \int_0^H \frac{S_{ref} - S(z)}{S_{ref}} dz,$$

where $S(z)$ is the salinity at depth z , and S_{ref} is the salinity at a given reference depth (cf. Gustafsson and Stigebrandt 1996).

The mixed layer depth, defined as the depth of the bottom of the upper homogeneous layer, was found from the density profile. The above-described estimates

all have the errors commonly associated with sparse resolution.

3. Hydrography, wind forcing, and buoyancy

The Baltic Sea is a semi-enclosed sea with virtually no tides because of the choking of exchange flow in the straits in the southwest. The annual runoff is 2% of the volume of the basin, and together with the restricted salinity input through the straits this creates a low salinity, between 6 and 7.5 in the surface layer of the Baltic proper. The mean horizontal circulation is weak and cyclonic, and follows the streamlines of the barotropic circulation (Fonselius 1996; Lehmann et al. 2002).

Figure 2 shows the (a) salinity, (b) temperature, and (c) density between August and October. The hydrography displays the typical seasonal pattern, with a shallow thermocline in summer that deepens during autumn. The thermocline resided at 15–20-m depth in the beginning of the record, which starts in early August (day 242 is 1 September). A baroclinic cyclonic eddy in the upper layers seemed to pass the area about day 253, lifting up colder and denser water toward the sea surface (Fig. 2). Between days 264 and 280, rapid thermocline erosion took place. At the beginning of October (day 274) the thermocline depth was around 32 m, deepening to 40 m and stabilizing at 45 m from the middle of October (day 280). The upper halocline and pycnocline coincided with the thermocline, and as temperature decreased, the vertical density gradient decreased. The perennial halocline was found between 60- and 70-m depth. The cold water between the upper pycnocline and the perennial halocline is the so-called old winter water.

The wind measured at the buoy is shown in Fig. 3. A weak peak of higher energy at the 48–50-h period was found from spectral analysis, but there are no evident dominant frequencies in the wind. The mean wind speed and standard deviation during August–October 2002 were 9 and 4.6 m s⁻¹, respectively. The lowest wind speeds were found in the beginning of the period, and wind speeds above 15 m s⁻¹ were found on a number of occasions. Figure 3b shows a progressive vector diagram of the filtered wind. The wind was mainly from the south-southwest in August (days 220–241), turning to north in mid-September (252), and to south in the end of October (day 294).

Figure 4a shows the 24-h filtered buoyancy flux (upper panel, m² s⁻³), and the cumulative buoyancy flux ($\int B dt$, m² s⁻²), both total and the contribution from heat and freshwater (bottom panel). Initially, the buoyancy flux was positive, but after day 240 the general trend

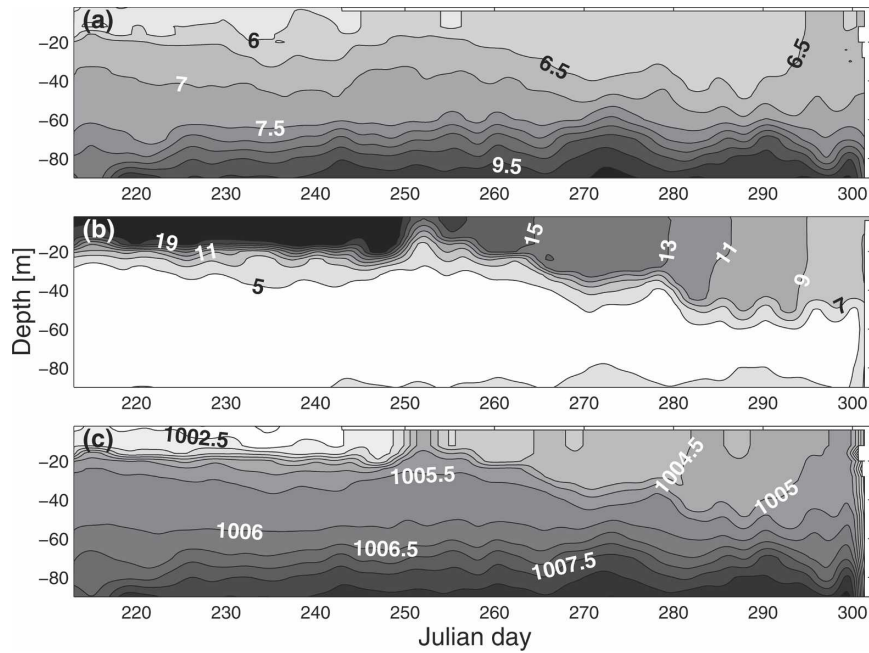


FIG. 2. (a) Salinity, (b) temperature ($^{\circ}\text{C}$), and (c) density (kg m^{-3}) at the SMHI buoy between early August and late October 2002. The data have been interpolated and filtered.

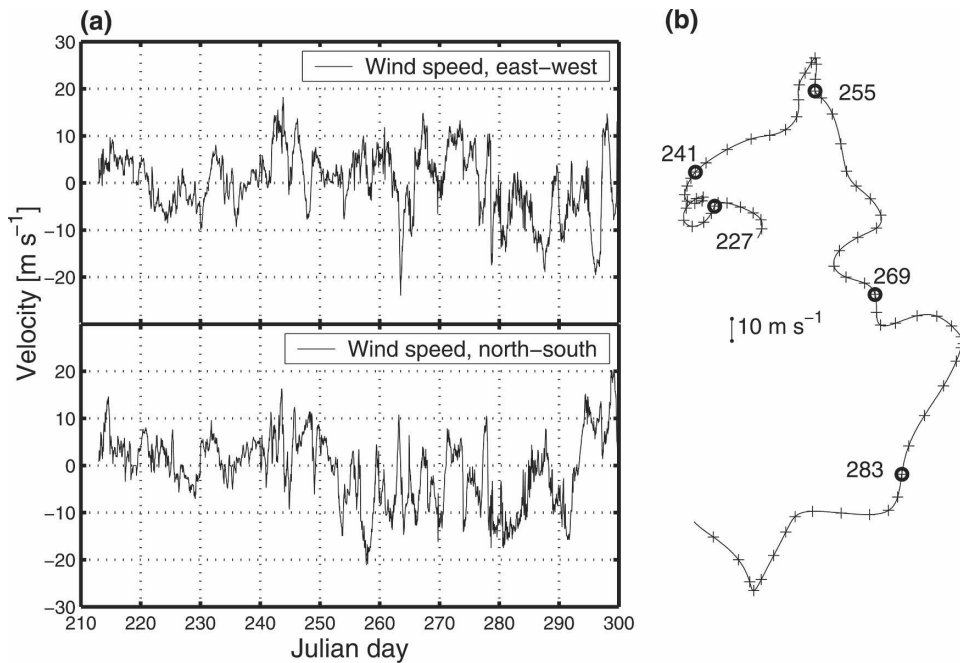


FIG. 3. (a) Observed unfiltered (top) east–west and (bottom) north–south components of the wind velocity observed at the SMHI buoy, and (b) cumulative, low-pass-filtered wind velocity, where the daily interval is marked with a cross and every 14 days with a circle, and north is upward. The velocity corresponding to 10 m s^{-1} during 1 day is shown in the figure.

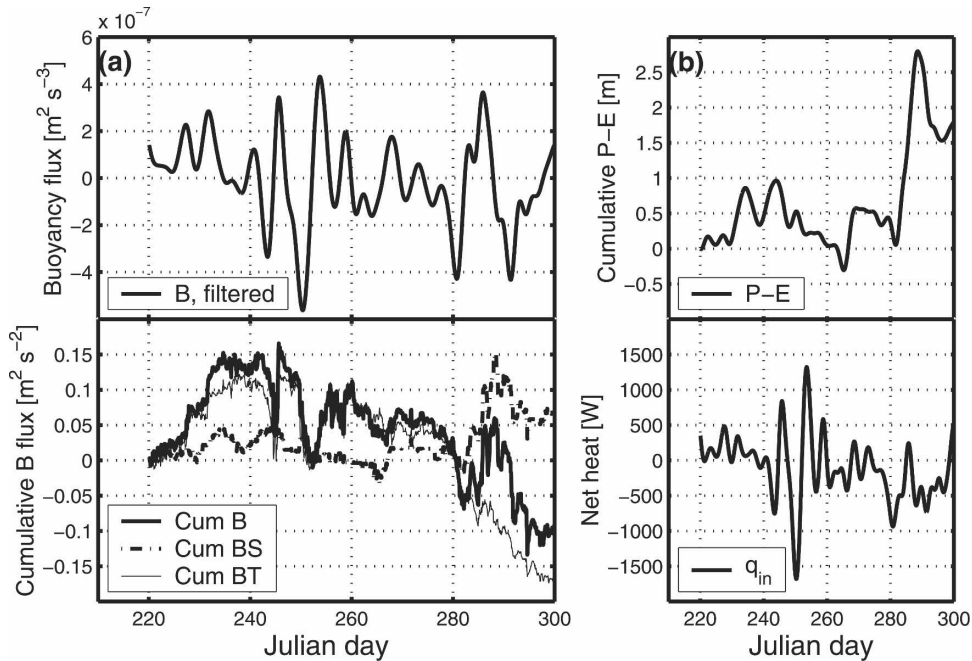


FIG. 4. (a) The (top) added buoyancy through the surface, filtered with a 24-h filter, and the (bottom) cumulative buoyancy Cum B with contributions from freshwater, Cum BS, and heat fluxes, Cum BT. (b) The (top) integrated contribution from $P - E$ and the (bottom) instantaneous heat flux.

was a negative buoyancy flux through the surface, with the exception of four periods: days 245–246, 252–255, 266–268, and 282–288. The large fluctuations around day 253 may partly be an artifact due to what appears to be an eddy. Figure 4b shows the integrated $P - E$ and the instantaneous heat flux through the sea surface. The buoyancy flux was dominated by heat fluxes, with the exception of days 281–288, when the so-called net precipitation ($P - E$) was positive and rather large. In the Baltic, 2002 was a uniquely dry year, with negative $P - E$ (Omstedt and Nohr 2004).

Figure 5 shows the observed depth of the mixed layer h_{ml} and the calculated Ekman and Monin–Obukhov depths, h_e and h_{mo} , respectively. The mixed layer depth followed the Ekman depth roughly in the first half of the measurement period. From day 262, the mixed layer became deeper than the Ekman depth. The Monin–Obukhov depth, defined only for positive B , was quite erratic since both the wind and especially B had high variability.

4. Current structure

Current measurements show that the velocity in the entire water column was dominated by inertial oscillations (Nerheim 2004). Here, the data have been low-pass filtered as described in section 2.

Figure 6 shows the current trajectories from selected levels (from filtered data), which gives the distance a water parcel passing the buoy would travel. The distance corresponding to 10 cm s^{-1} during 1 day is displayed. The following selected depths are shown: (a) 4, (b) 20, (c) 40, and (d) 70 and 90 m. The 4-m measurement represents the upper 16 m well, though higher variability was found at the 2-m level. The 20-m measurement is representative for the 20–32-m level. The 40-m measurement represents the 36–48-m level, and the 70-m level is representative for the current between 50 and 70 m. The current at 80 and 90 m, that is, in the halocline, is more variable and probably affected by both bottom friction and baroclinic effects. The possible baroclinic eddy seen around day 250 in the hydrography was not obvious from the velocity measurements.

The mean speed was $0.07\text{--}0.1 \text{ m s}^{-1}$, the weakest currents found at 2 and 80–90 m. The vertical homogeneity in the current indicated that a significant part of the current was barotropic. In the following analysis, the barotropic component, or reference velocity, was taken to be the current velocity in the so-called winter water above the perennial halocline but below the upper pycnocline. The 40-m level was chosen as reference level, and the current at this level was subtracted from the current at all depths. The residual current in the surface

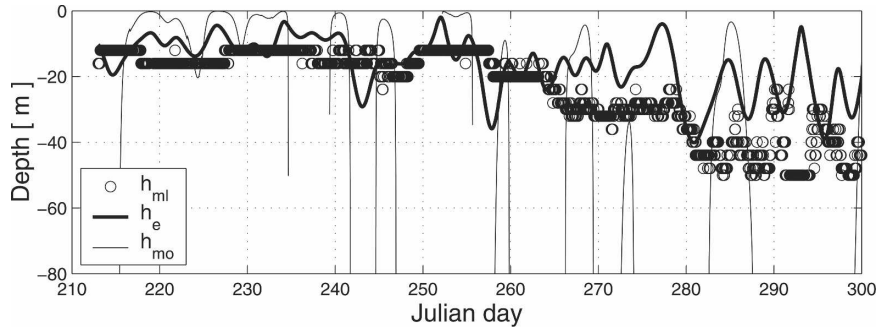


FIG. 5. The observed mixed layer depth h_{ml} , the calculated Ekman depth h_e , and the Monin-Obukhov depth h_{mo} , estimated from the friction velocity and buoyancy fluxes.

layers is (one hopes) mainly the wind-driven part of the current. This treatment neglects possible baroclinic currents. Unfortunately, because of the lack of hydrographic data from the area surrounding the buoy during this time, this bias cannot be properly assessed. After day 280, the thermocline went below 40 m (see Fig. 5), and from then on the 50-m level was used as reference level. Because of the uniformity of the current, the fol-

lowing calculations were not influenced unduly by this, and using the 50-m level throughout gave small changes in the calculated transport.

After removing the reference velocity from all depths, the residual current in the old winter water down to 70 m was quite small, whereas the remaining current in the surface and bottom layer was larger. For a more thorough investigation of a possible baroclinic

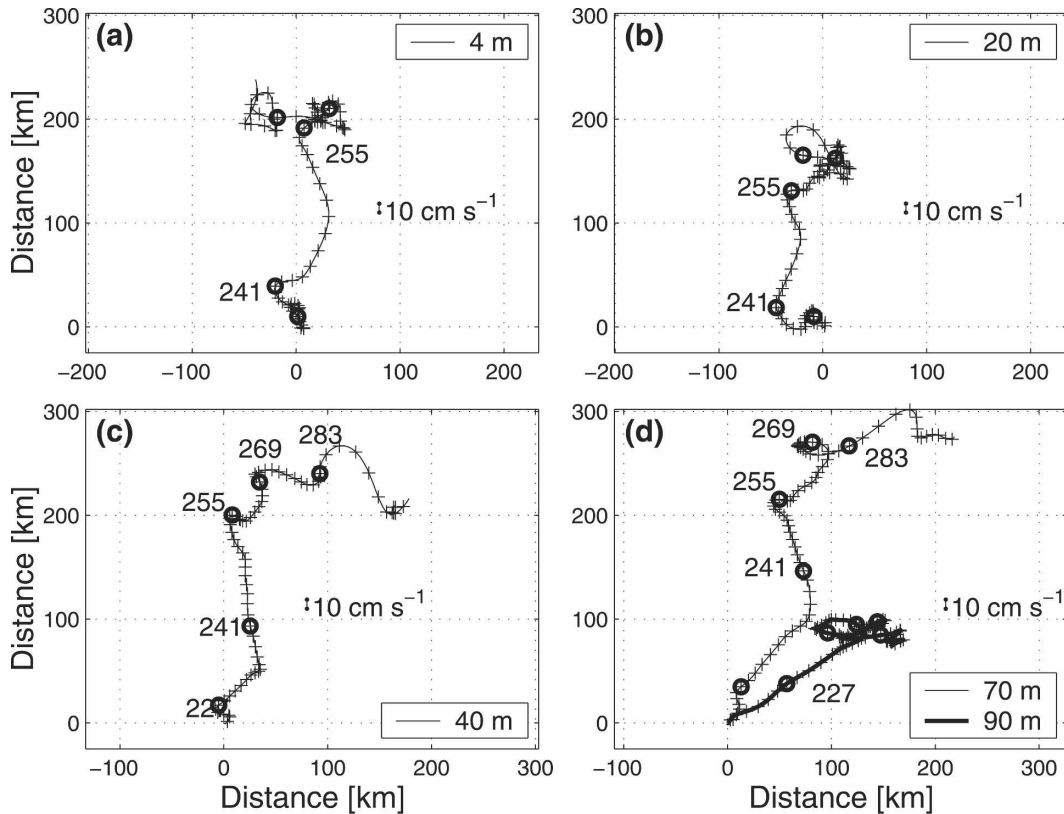


FIG. 6. Current trajectories of the levels (a) 4-, (b) 20-, (c) 40-, (d) 70-, and 90-m depth. Crosses show daily values, and circles every 14 days; north is upward. The vertical bar shows the equivalent distance traveled in 1 day with a current speed of 10 cm s^{-1} . Numbers for the circled observations refer to year day.

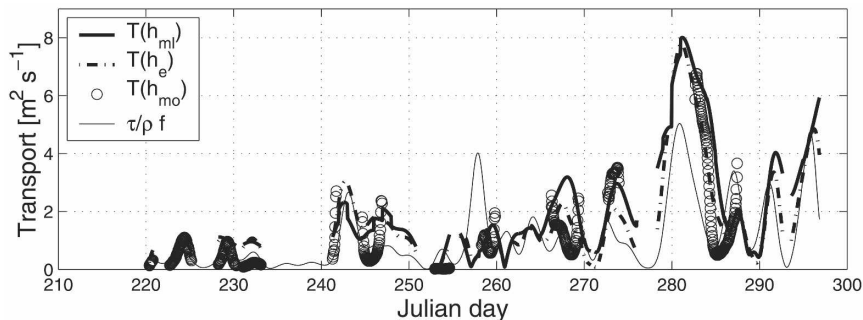


FIG. 7. Transport of the wind-driven upper layer ($\text{m}^2 \text{s}^{-1}$) for the mixed layer, the Ekman depth, the Monin–Obukhov depth, and the theoretical Ekman transport $\tau/\rho f$.

component, at least three different hydrographic stations would be desirable. The available hydrographic data from the past two decades in BED were used to confirm that the area is horizontally very homogeneous during this time of year, giving small baroclinic contributions (not shown).

It is well known that in coastal areas alongshore winds may give rise to alongshore jets (e.g., Csanady 1982; Lass and Talpsepp 1993; Ohlmann and Niiler 2001). Lass and Talpsepp (1993) showed that the coastal barotropic boundary current in the southern Baltic extended two baroclinic Rossby radii out from the coast. Following Ohlmann and Niiler (2001) and rotating the coordinate system in a cross-shore and an alongshore direction, the possibility of such a coastal jet was ruled out in the present case. There was no connection between alongshore winds and alongshore acceleration, nor any other discernible bias in the response due to the proximity of the coast, and thus this contribution was assumed to be negligible. Last, possible semiperiodic phenomena like Kelvin waves and seiches were ruled out in Nerheim (2004), in which the dominant time scales in the Baltic proper were investigated. The effects from Stokes drift on the transport calculations were found to be negligible, and wave bias has also been ruled out.

5. Transport estimates

The wind drift current (u, v) was estimated from measurements as described in section 4 above. The volume transports of the wind drift in the east–west and north–south directions were found by integrating the velocity u and v over a surface layer H :

$$U = \int_{-H}^0 u \, dz \quad \text{and} \quad V = \int_{-H}^0 v \, dz. \quad (8)$$

Each of the three layer-thickness estimates (the observed mixed layer h_{mi} , the Ekman depth h_e , and the

Monin–Obukhov depth h_{mo}) were used for H in Eq. (8).

The transport $T = \sqrt{U^2 + V^2}$ was compared with the theoretical wind driven transport in homogeneous water $\tau/\rho f$, since (Ekman 1905)

$$\rho f U_E = \tau_y \quad \text{and} \quad \rho f V_E = -\tau_x, \quad (9)$$

where U_E and V_E denote the theoretical wind-driven transport in the x and y directions, with the common Cartesian directions with positive x to the east and positive y to the north. Since the signal-to-noise ratio is quite low for low wind speeds, only data for cases with $W \geq 5 \text{ m s}^{-1}$ were used to study the statistics of direction and magnitude of the observed transport. Figure 7 shows the observed transports from the mixed layer depth h_{mi} , the Ekman depth h_e , and the Monin–Obukhov depth h_{mo} for $W \geq 5 \text{ m s}^{-1}$, together with the theoretical transport $\tau/\rho f$. The three observed transport estimates deviate from each other and the theoretical transport from time to time. The largest difference between the observed and theoretical transport is seen in the period of erosion and strong winds toward the end of the period, when the transport estimated from the Ekman depth and the mixed layer depth are quite similar despite the different depths (Fig. 5).

Following Stigebrandt (1985), the smallest of the three depths (h_{mi} , h_e , and h_{mo}) were chosen at times of positive and h_{mi} at times of negative buoyancy flux. The resulting observed transport is shown in Fig. 8 together with the theoretical transport. The fit is for the most part reasonably good, although the observed transport is generally greater than the theoretical transport. The direction of the transport θ_t and the wind stress θ_w (in degrees) is plotted in Fig. 8 (bottom). While the wind rotates slowly clockwise, the current seems to be rotating counterclockwise. The direction of the wind, and also the transport, is fairly constant when the wind speeds are high, for instance during days 270–285.

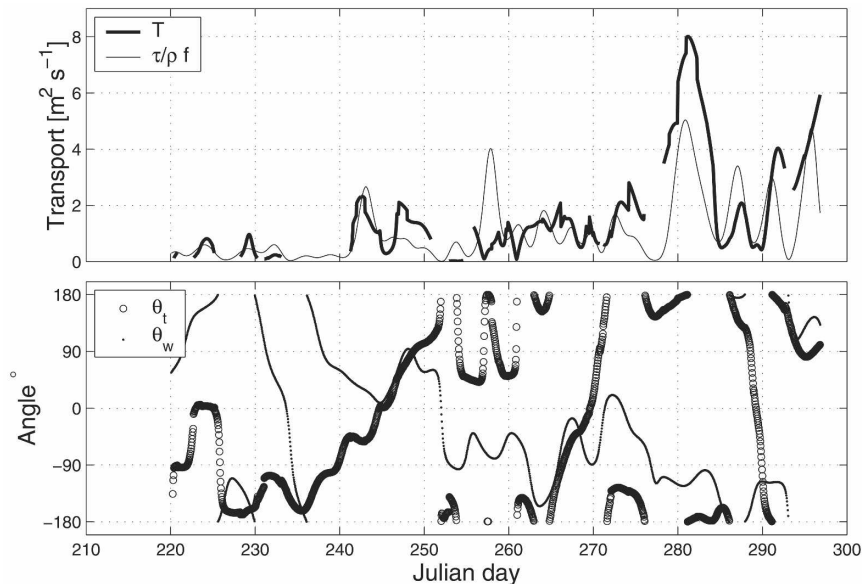


FIG. 8. (top) The observed wind-driven transport (thick line) for the length scale chosen according to Stigebrandt (1985) and the theoretical transport (solid line). (bottom) The direction of the wind θ_w and the direction of the transport θ_T .

After removing the cases with $W < 5 \text{ m s}^{-1}$, the resulting data, approximately 1500 measurements with hourly sampling, were separated into four regimes. For negative buoyancy fluxes through the surface, the mixed layer depth is the valid depth of the wind drift (ML-1). The three regimes for positive buoyancy flux are the Monin–Obukhov (MO) regime, the Ekman depth (E) regime, and a second mixed layer (ML-2) regime. The four regimes occur during 53%, 35%, 9%, and 3% of the time, respectively. Figure 9 shows the direction of the transport relative to the wind, $\theta_w - \theta_T$. In the upper panel a stacked histogram of all four regimes establishes that the transport was chiefly to the right of the wind. The mean transport deflection for the interval $(-45^\circ, +135^\circ)$ was 55° rather than the theoretical value of 90° . The four bottom panels show the four different regimes. The transport during negative buoyancy fluxes (ML-1) was concentrated to the 45° – 90° sector. For the MO regime, the wind current shifted closer to the direction of the wind. The E regime and the ML-2 regime occurred fewer times, the ML-2 regime tentatively displaying similarities with the MO regime. The E regime had a larger deflection than 90° , and a larger spread.

To further substantiate the claims that the topographic effects are negligible, the coordinate system was rotated and the distribution studied with respect to alongshore and cross-shore winds, and with respect to alongshore and cross-shore mean currents. There is a slight tendency for a “best” Ekman-type deflection for

winds from the northeast along the coast, and from the northwest perpendicular to the coast, where the above-presented relationships are very clear. Winds from the southwest along the shore, or from the southeast, lead to flatter (more noisy) distributions. These cases are found less often, and the larger scatter is probably due to the lack of stationarity, which is more pronounced for the less-often-occurring winds. To assess any possible topographic effects on the total current, the same analysis was performed for the data before removal of the reference velocity, but no significant effect or coastal response was found. Thus, the proximity of the coast and the topography seems to have little impact on the wind drift or the total current at the buoy.

Figure 10 (top) shows the ratio between the observed and theoretical transports

$$R_T = \frac{T}{\tau/\rho f}, \quad (10)$$

calculated for 24-h periods. The mean value for R_T is 1.38, and the theoretical transport thus underestimates the observed. In the lower panel, the 24 h averaged buoyancy flux is shown. The magnitude of the buoyancy flux was not found to affect R_T directly. Distinguishing again between the four different regimes, the period of negative buoyancy flux, ML-1, has a mean R_T value of 1.69. During positive buoyancy flux, the MO, E, and ML-2 regimes have mean R_T values of 0.77, 1.72,

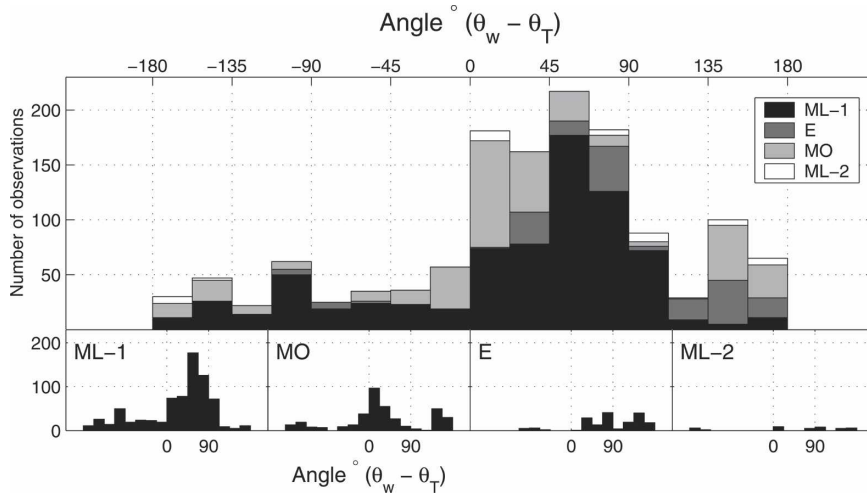


FIG. 9. Histogram over the angle of the transport relative to the direction of the wind stress for $W \geq 5 \text{ m s}^{-1}$. Positive values for deflection to the right of the wind. (top) The stacked distribution for all measurements. (bottom) The four wind-layer regimes: one during negative buoyancy flux [mixed layer depth (ML-1)], and the three possible regimes during positive buoyancy flux [the Monin–Obukhov depth (MO), Ekman depth (E), and a second mixed layer depth (ML-2)].

and 0.73, respectively. The standard deviation of R_T was largest for ML-1 and E.

A small number of occurrences with disparate observed transports in comparison with theory lead to augmented values of the ratio R_T . These few occurrences are mainly found during periods of deep convecting layers when a negative buoyancy flux coincides with high winds (from day 278 and onward). High-wind events or regions of higher winds are likely to be responsible for most of the energy input to the Ekman layer (e.g., Wang and Huang 2004). High-wind-speed events during negative buoyancy fluxes emerge as an

aspect of the wind current dynamics that needs to be further assessed.

Wind energy input

Since the direction of the observed wind-forced current is rather uniform (slablike), the wind-parallel surface current can be approximated as the wind-parallel transport T_w divided by the depth H of the current. From Eq. (5), T_w is given by $T_w = R_T \tau / \rho f \cos(\theta_w - \theta_t)$, where $\cos(\theta_w - \theta_t)$ is the decomposition of the observed transport to the wind’s direction, found from Fig. 9. For positive B , $R_T = 0.77$ and $(\theta_w - \theta_t) = 30^\circ$; for

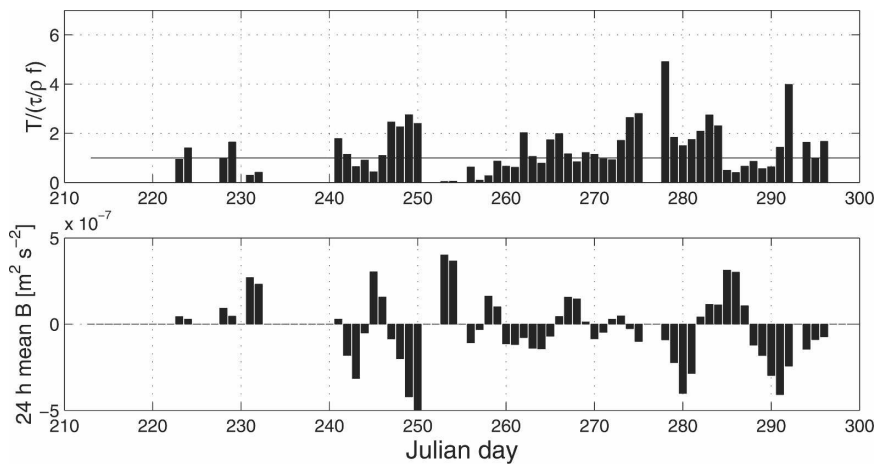


FIG. 10. (top) The ratio R_T between observed T and theoretical $\tau / \rho f$, for 24-h averaged values and (bottom) 24-h averaged buoyancy flux. Only days with $W \geq 5 \text{ m s}^{-1}$ are shown.

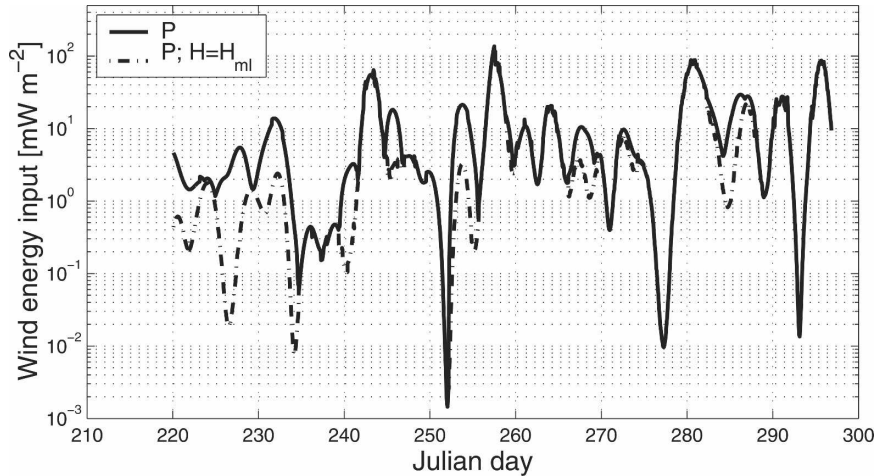


FIG. 11. Values of P for H determined from the three different regimes and from $H = h_{ml}$.

negative B , $R_T = 1.69$ and $(\theta_w - \theta_t) = 60^\circ$. The energy input from the wind stress to the surface layer then equals

$$P = \tau \frac{T_w}{H}. \quad (11)$$

Figure 11 shows P for two different choices of H , first for the same choice of H as used for the transport calculations, namely, the different wind-layer regimes; P is in the range 0.001 – 100 mW m^{-2} , and the total mean P is 11.99 mW m^{-2} . For $B > 0$, the mean of P is 9.58 mW m^{-2} , and for $B < 0$, 14.31 mW m^{-2} . Part of the reason for the higher values during negative buoyancy fluxes is a higher average wind stress in that time period. In the second calculation the observed mixed layer depth is used for H . This gives lower values during the periods when the Monin–Obukhov length regime is valid and the wind current is shallow.

Wang and Huang (2004) used National Centers for Environmental Prediction (NCEP)–National Center for Atmospheric Research (NCAR) data to calculate the energy input from the low-pass-filtered wind stress to the Ekman layer. They found a global mean energy input equal to 6.4 mW m^{-2} , with the main input concentrated over the Southern Ocean and storm tracks in the North Atlantic and North Pacific. This is a factor of 2 lower than our estimate for some months in the Baltic.

6. Discussion

The interpretation in this study is based on an assumption of a current that mainly consists of a barotropic and a wind-driven surface component. A topographic response was not found, but the question of a baroclinic component stays unresolved because of lack

of hydrographic data with spatial resolution. Nevertheless, the fact remains that the four different buoyancy regimes displayed quite different characteristics when the barotropic component was removed, and that is what lead to the hypothesis and interpretation presented here and below.

For the observations as a whole, the results may be interpreted as follows. An observed wind-driven transport T in the sector $(\theta_w - \theta_t \leq 90^\circ)$ indicates that there is a transport component parallel to the wind equal to $T \cos(\theta_w - \theta_t)$. From the normal component $T \sin(\theta_w - \theta_t)$ one obtains the “Ekman” component,

$$R_{TN} = \frac{T \sin(\theta_w - \theta_t)}{\tau/\rho f}. \quad (12)$$

For instance, with $\theta_w - \theta_t = 60^\circ$ one obtains $R_{TN} = 1.20$ (overall mean). With this interpretation, the classical result of Ekman is still overestimated for the transport perpendicular to the wind in addition to the component parallel to the wind. This is illustrated in Fig. 12. Such a component should arise, for instance, if the wind-driven current is subjected to flow resistance (stress) at the (seasonal) pycnocline. The vertically integrated force balance of the wind-driven current now involves not only surface stress and the Coriolis force, as in classical Ekman theory, but also a bottom stress. This inevitably gives a flow component in the direction of the wind.

A wind-parallel component has been reported also by other authors. Schudlich and Price (1998) found a persistent downwind shear in the upper 15 m during winter measurements, though not during summer, and the mean observed transport during winter exceeded the theoretical by a large fraction. Krauss (1993) calculated a viscosity tensor to relate stress and vertical

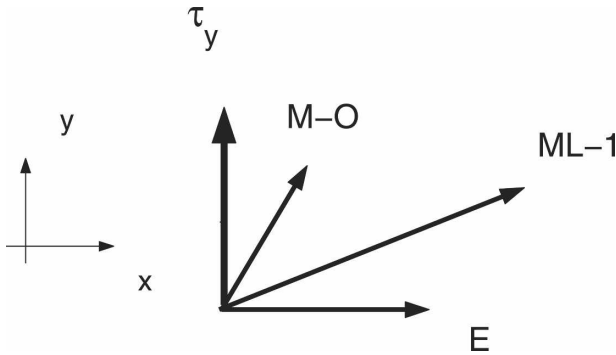


FIG. 12. The Ekman transport perpendicular to the wind stress, together with the transport observed in the ML-1 and MO regimes.

shear, and found maximum values at 15–20 m, interpreted as a result of Langmuir circulation. The stresses varied with depth, from 10° to the right of the wind near the surface to 50° at 25-m depth. Stacey et al. (1986) defined a deep wind-current layer from velocity eigenfunctions and suggested that tidally generated turbulence may increase the depth to which wind-induced momentum may diffuse. They suggested that the observed 79° deflection to the right of the wind, rather than 90° , was caused by, for instance, tidal influence, experiment setup, or topographic effects. A common source of error in the previous cited works is the use of a linear drag coefficient (Chereskin and Roemmich 1991; Schudlich and Price 1998; Price and Sundermeyer 1999). Large and Pond (1981) estimated the error in the

wind stress approximations due to the drag coefficient to be as high as 20%. In the present case, the boundary layer estimated drag coefficient was a factor 1.2 times larger than the bulk formula.

Provided that the weaker deflection of the current than the expected 90° is explained by a stress at the boundary, models invoking a bottom stress may be useful to understand these observations. Two such models are discussed in the following.

Ekman (1905) also treated pure drift currents in an ocean of finite depth, showing that for depths larger than 1.25 times the frictional depth D_E , the solutions for finite and infinite depths converge. Ekman's depth of frictional influence,

$$D_E = \pi \sqrt{\frac{2A_z}{f}}, \quad (13)$$

where A_z is the vertical diffusivity, is equal to 3.25 times the Ekman depth h_e defined earlier if

$$A_z = 3.25^2 \frac{\kappa^2 C_d W^2 \rho_a}{2\pi^2 f \rho}. \quad (14)$$

With $\kappa = 0.2$, $C_d = 2 \times 10^{-3}$, $\rho_a = 1.4 \text{ kg m}^{-3}$, $\rho = 10^3 \text{ kg m}^{-3}$, and $f = 1.2 \times 10^{-4} \text{ s}^{-1}$, one obtains $A_z = 5 \times 10^{-4} \times W^2 \text{ m}^2 \text{ s}^{-1}$. This formula gives values for A_z close to those given in Neumann and Pierson (1966, table on p. 195).

Following Neumann and Pierson (1966), for an ocean of depth d , the bottom boundary conditions are $u, v = 0$ for $z = d$. Then, the integrated mass transport $\rho \times T_{x,y}$ is equal to

$$\rho T_x = \frac{\tau_y}{f} \frac{\cosh 2\frac{a}{\sqrt{2}}d + \cos 2\frac{a}{\sqrt{2}}d - 2 \cosh \frac{a}{\sqrt{2}}d \cos \frac{a}{\sqrt{2}}d}{\cosh 2\frac{a}{\sqrt{2}}d + \cos 2\frac{a}{\sqrt{2}}d} \quad \text{and} \quad (15)$$

$$\rho T_y = \frac{\tau_x}{f} \frac{\sinh \frac{a}{\sqrt{2}}d \sin \frac{a}{\sqrt{2}}d}{\cosh 2\frac{a}{\sqrt{2}}d + \cos 2\frac{a}{\sqrt{2}}d}, \quad (16)$$

where τ_y is the wind stress (to the north) and $a^2 = f(\rho/A_z)$. Figure 13a shows the amplification factor for the two components for $d = KD_E$, with K ranging from 0 to 1.35. For $K = 0.5$ the amplification in the x direction is equal to 1; the total transport is $1.02\tau/\rho f$, 79° to the right of the wind, as compared with 90° for infinite depth. For a two-layer model, the analogy with the finite-depth model explains the observed $\sim 60^\circ$ deflection

when $d = 0.32D_E \approx h_e$. The corresponding total transport is $0.6\tau/\rho f$, which is a factor of 2.3 smaller than the ML-1 regime and also is smaller than the mean of all four regimes. A deflection of 30° , as observed in the MO regime, corresponds theoretically to a transport of $0.19\tau/\rho f$, which is about one-fourth of the observed transport in that regime.

Our observations show that the wind-driven mixed layer has velocity characteristics much like a slab. Applying a stationary slab model,

$$-fv = \frac{\tau_x}{H\rho} - Cu \quad \text{and} \quad fu = \frac{\tau_y}{H\rho} - Cv, \quad (17)$$

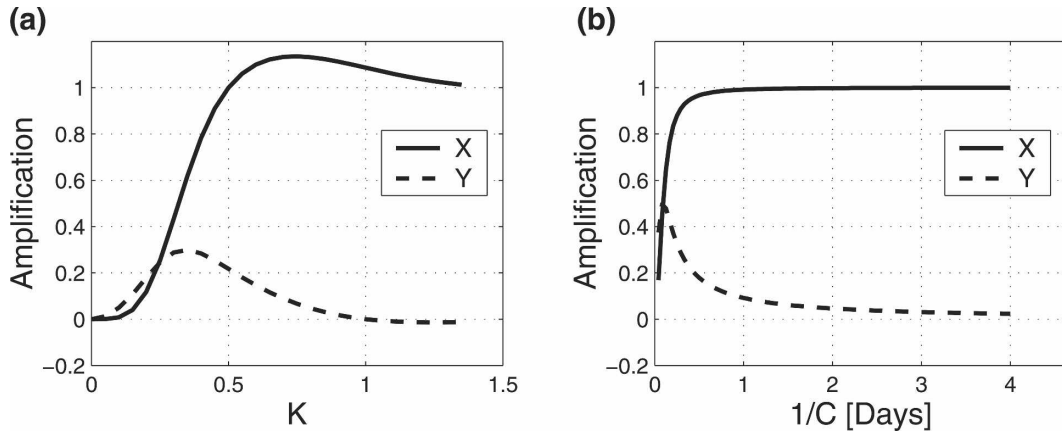


FIG. 13. The changes in transport due to (a) finite depth and (b) bottom drag in a slab model. Here, K is the depth normalized by the friction depth, $d = KD_E$, and C is the linear drag coefficient.

somewhat different transport relations appear. Here, u and v are the velocities of the slab, H the depth of the mixed layer, and C the linear drag coefficient corresponding to the decay time scale C^{-1} . Using again $\tau = \tau_y$, the relationship between $(U, V) = (u, v)H$ and $\tau/\rho f$ gives the following modification of the wind-driven transport due to the bottom drag:

$$U = \frac{f^2}{f^2 + C^2} \frac{\tau}{\rho f} \quad \text{and} \quad V = \frac{fC}{f^2 + C^2} \frac{\tau}{\rho f}. \quad (18)$$

The amplification factors for U and V are plotted for $0 < C^{-1} < 4$ days in Fig. 13b. The total transport goes asymptotically toward 1. A deflection of 60° to the right of the wind corresponds to a total transport near $0.87\tau/\rho f$, that is, greater than the theoretical Ekman transport in the same direction for shallow layers but smaller than the observed transport. A deflection of 30° gives a transport of $0.49\tau/\rho f$. The C values are then 4 and 1.3 h, respectively. These values are not chosen for any physical rationale but may be interpreted as a short response time between a bottom stress and a resulting wind-parallel component.

In conclusion, the observed transport in the ML-1 regime ($B < 0$), $1.69\tau/\rho f$, directed about 60° to the right of the wind, can be explained by neither the finite-depth equations nor the slab model. For shallow layers in the MO and ML-2 regimes ($B > 0$) the observed transport was $\approx 0.75\tau/\rho f$, directed about 30° to the right of the wind. This result is reasonably well predicted by the slab model if $C \approx 1.3 \text{ h}^{-1}$. The finite-depth equations underestimate the transport in this case.

Though the models outlined here do not fully explain the observed transports, they may be suggestions for further development of new boundary conditions that closer resemble the true wind drift found in the sea.

Neither model takes the buoyancy effects into account. It is not unlikely that turbulence effects and small-scale mixing may have unknown impacts on the current. Hosegood and van Haren (2003) found a spike-like reduction in current speed associated with concurrent deflections in the current direction in the mainly geostrophic current on the continental slope of the Faeroe–Shetland Channel. They found that the change in current was associated with intermittent bursts of turbulence, explained by a bursting phenomenon in a bottom boundary layer caused by the thickening of the boundary layer due to a downslope Ekman transport of buoyancy. This is in accordance with the speculations on tidally generated turbulence found in Stacey et al. (1986). Similar small-scale effects that differ depending on the sign of the surface buoyancy flux may explain the observed differences between regimes.

7. Concluding remarks

The sign of sea surface buoyancy fluxes appears to be crucial in determining the characteristics of the wind-current transport. Drag at the bottom of the wind-current layer will give rise to a component parallel to the wind, whose magnitude depends critically on the sign of the buoyancy flux.

The classical Ekman regime, with homogeneous water and vanishing buoyancy fluxes, is realized only about 10% of the time in the present investigation. Most of the time, buoyancy fluxes through the sea surface causes the well-mixed layer to be either shallower or deeper than the classical Ekman depth. In both cases there is a wind-parallel transport component in the mixed layer. This is obviously coupled to stress acting at the bottom of the well-mixed surface layer that causes

transfer of momentum and power to the water below the well-mixed layer. The results in the regime of positive buoyancy fluxes with a relatively thin well-mixed layer seem to be explained qualitatively by the so-called slab model. However, neither of the simple models explains the results for the case of negative buoyancy fluxes, causing enhanced vertical exchange in the surface layer due to thermohaline convection. In particular, the large wind-parallel transport component occurring in this case is not explained. Such a component should have great importance on ocean circulation if generally applicable.

It seems that there is a severe lack of knowledge regarding the influence of small-scale thermohaline convection upon the wind drift. This should be a common situation in the ocean, maybe 50% of all instances, which should motivate increased research efforts upon this old and partly petrified part of physical oceanography. Longer datasets with longer periods of positive and negative buoyancy fluxes, and also longer quasi-stationary periods, would be of interest to improve the analysis and the understanding of the wind drift leading to development of a better process-based model of the wind drift.

Acknowledgments. The authors thank SMHI for providing the data and Stockholm University for maintaining the Baltic Environmental Database. We are also grateful to two anonymous reviewers for constructive and helpful comments on an earlier version of this paper.

REFERENCES

- Arya, S. P., 1988: *Introduction to Micrometeorology*. Academic Press, 307 pp.
- Carlsson, M., 1998: A coupled three-basin sea level model for the Baltic Sea. *Cont. Shelf Res.*, **18**, 1015–1038.
- Chereskin, T. K., 1995: Direct evidence for an Ekman balance in the California current. *J. Geophys. Res.*, **100** (C9), 18 261–18 269.
- , and D. Roemmich, 1991: A comparison of measured and wind-derived Ekman transport at 11°N in the Atlantic Ocean. *J. Phys. Oceanogr.*, **21**, 869–878.
- Csanady, G. T., 1982: *Circulation in the Coastal Ocean*. D. Reidel, 279 pp.
- Davis, R. E., R. deSzoeko, D. Halpern, and P. Niiler, 1981: Variability in the upper ocean during MILE. Part I: The heat and momentum balances. *Deep-Sea Res.*, **28A**, 1427–1452.
- Ekman, V., 1905: On the influence of the earth's rotation on ocean currents. *Arkiv. Mat., Astron. Fys.*, **11**, 1–52.
- Fonselius, S., 1996: Västerhavets och Östersjöns oceanografi. SMHI Publ.
- Gustafsson, B., and A. Stigebrandt, 1996: Dynamics of the freshwater-influenced surface layers in the Skagerrak. *J. Sea Res.*, **35**, 39–53.
- Hosegood, P., and H. van Haren, 2003: Ekman-induced turbulence over the continental slope in the Faroe-Shetland Channel as inferred from spikes in current meter observations. *Deep-Sea Res. I*, **50**, 657–680.
- Krauss, W., 1993: Ekman drift in homogeneous water. *J. Geophys. Res.*, **98**, 20 187–20 209.
- Large, W. G., and S. Pond, 1981: Open ocean momentum flux measurements in moderate to strong winds. *J. Phys. Oceanogr.*, **11**, 324–336.
- Lass, H. U., and L. Talpsepp, 1993: Observations of coastal jets in the Southern Baltic. *Cont. Shelf Res.*, **13**, 189–203.
- Launiainen, J., 1995: Derivation of the relationship between the Obukhov stability parameter and the bulk Richardson number for flux profiles. *Bound.-Layer Meteor.*, **76**, 165–179.
- Lehmann, A., W. Krauss, and H.-H. Hinrichsen, 2002: Effects of remote and local atmospheric forcing on circulation and upwelling in the Baltic Sea. *Tellus*, **54A**, 299–316.
- Liljebladh, B., and A. Stigebrandt, 1996: Deepwater flow into the Baltic Sea. *J. Geophys. Res.*, **101** (C4), 8895–8911.
- Nerheim, S., 2004: Shear-generating motions at various length scales and frequencies in the Baltic Sea—An attempt to narrow down the problem of horizontal dispersion. *Oceanologia*, **46**, 477–503.
- Neumann, G., and W. J. Pierson, 1966: *Principles of Physical Oceanography*. Prentice Hall, 545 pp.
- Niiler, P. P., and J. D. Paduan, 1995: Wind-driven motions in the northeast Pacific as measured by Lagrangian drifters. *J. Phys. Oceanogr.*, **25**, 2819–2830.
- Ohlmann, J. C., and P. P. Niiler, 2001: A two-dimensional response to a tropical storm on the Gulf of Mexico shelf. *J. Mar. Syst.*, **29**, 87–99.
- Omstedt, A., and C. Nohr, 2004: Calculating the water and heat balances of the Baltic Sea using ocean modeling and available meteorological, hydrological and ocean data. *Tellus*, **56**, 400–414.
- Price, J. F., and M. A. Sundermeyer, 1999: Stratified Ekman layers. *J. Geophys. Res.*, **104** (C9), 20 467–20 494.
- , R. A. Weller, and R. R. Schudlich, 1987: Wind-driven ocean currents and Ekman transport. *Science*, **238**, 1534–1538.
- Schudlich, R., and J. Price, 1998: Observations of seasonal variation in the Ekman layer. *J. Phys. Oceanogr.*, **28**, 1187–1204.
- Stacey, M. W., S. Pond, and P. H. LeBlond, 1986: A wind-forced Ekman spiral as a good statistical fit to low-frequency currents in a coastal strait. *Science*, **233**, 470–472.
- Stigebrandt, A., 1985: A model for the seasonal pycnocline in rotating systems with application to the Baltic proper. *J. Phys. Oceanogr.*, **15**, 1392–1404.
- Wang, W., and R. X. Huang, 2004: Wind energy input to the Ekman layer. *J. Phys. Oceanogr.*, **34**, 1267–1275.